Elucidating Interfacial Limitations Induced by Tin Oxide Electron Selective Layer Grown by Atomic Layer Deposition in N–I–P Perovskite-Based Solar Cells

Félix Gayot, Elise Bruhat, Muriel Bouttemy, Mathieu Frégnaux, Eric de Vito, Jean-Paul Kleider, Stéphane Cros, Matthieu Manceau

▶ To cite this version:

Félix Gayot, Elise Bruhat, Muriel Bouttemy, Mathieu Frégnaux, Eric de Vito, et al.. Elucidating Interfacial Limitations Induced by Tin Oxide Electron Selective Layer Grown by Atomic Layer Deposition in N–I–P Perovskite-Based Solar Cells. ACS Applied Energy Materials, 2023, 6 (23), pp.11849-11860. 10.1021/acsaem.3c01713 . hal-04373337

HAL Id: hal-04373337
https://hal.science/hal-04373337v1

Submitted on 25 Nov 2024

Elucidating Interfacial Limitations Induced by an ALD-grown Tin Oxide Electron Selective Layer in N-I-P Perovskite-Based Solar Cells

Félix Gayot[1,2], Elise Bruhat[1,2], Muriel Bouttemy[4], Mathieu Frégnaux[4], Eric De Vito[3], Jean-Paul Kleider[5,6], Stéphane Cros[1,2], Matthieu Manceau[1,2]*

[1] Univ. Grenoble Alpes, INES, F-73375 Le Bourget du Lac, France

[2] CEA Liten, Department of Solar Technologies, F-73375 Le Bourget du Lac, France

[3] Univ. Grenoble Alpes, CEA Liten, Department of Nanomaterial technologies, 38054 Grenoble Cedex, France

[4] Institut Lavoisier de Versailles (ILV), UMR CNRS-UVSQ 8180, Université Paris-Saclay, 45 av. des Etats-Unis, 78035 Versailles Cedex, France

[5] Université Paris-Saclay, CentraleSupélec, CNRS, Laboratoire de Génie Electrique et Electronique de Paris, 91192, Gif- sur-Yvette, France

[6] Sorbonne Université, CNRS, Laboratoire de Génie Electrique et Electronique de Paris, 75252, Paris, France

* felix.gayot@protonmail.com

KEYWORDS. Electron Transport Layer, Atomic Layer Deposition, SnO_2, Perovskite, Photovoltaics, Solar Cells

ABSTRACT. Fabricating tin dioxide (SnO_2) electron selective layers (ESL) by Atomic Layer Deposition can be of high interest for perovskite-based solar cells development since it offers a number of advantages over solution-based processes. However, ALD-grown SnO_2 ESL has been usually reported to yield limited cell efficiency compared to solution-processed SnO_2 ESL, without the causes being clearly identified. This is why we here conduct a thorough interface study using a set of complementary techniques. For this purpose, ALD-grown SnO_2 thin films are characterized in a systematic comparison with a reference solution-processed SnO_2. Energetics analysis by Ultraviolet Photoelectron Spectroscopy (UPS) points out an unfavorable band bending at the ALD-grown SnO_2/perovskite interface. Chemical characterization by Time-of-Flight Secondary Ion Mass Spectroscopy (ToF-SIMS) and Hard X-ray Photoelectron Spectroscopy (HAXPES) profiling unveils an unexpected lack of oxygen at ALD-grown SnO_2/perovskite interface, which may play a direct role in observed performance limitations.

I. INTRODUCTION

Perovskite (Pvk) solar cells are highly promising third-generation photovoltaic devices due to Pvk material outstanding optoelectronic properties [1–3]. Nowadays, after an exceptionally quick increase in efficiencies over the last decade, state-of-the-art Pvk solar cells reach power conversion efficiencies above 25% at lab scale [4]. There are several possible device architectures to fabricate such Pvk solar cells, depending on the stacking order of charge selective layers that are interfacing the Pvk film. Today, tin dioxide (SnO_2) is a commonly used material to fabricate such ESL, thanks to its N-type nature, its reported high electronic mobility and electron extraction rate, its large bandgap associated with high transparency in the visible range, and its relative chemical stability [5–7]. Up to now, the record efficiency for Pvk solar cells integrates a SnO_2 ESL [8]. Although

SnO_2 thin films can be deposited according to various fabrication routes, in state-of-the-art Pvk-based solar cells SnO_2 ESL are mainly deposited using sol-gel methods or nanoparticles dispersion via spin-coating [8,9]. To develop efficient large-areas Pvk solar cells, various processing routes to replace spin-coating are investigated, such as chemical bath deposition (CBD) or sloat-die coating [10–12]. It is worthwhile noticing that among them, CBD of SnO_2 thin films has recently shown strong improvements for a valuable application in Pvk solar cell fabrication. If primarily employed combined with a prior spin-coating step [11] or with relatively limited efficiency [10], more recent studies showed high-efficiency Pvk solar cells with an optimized one-step CBD SnO_2 ESL [9,13,14], with a champion device showing a state-of-the-art power conversion efficiency of 25.2% fabricated by Yoo and coworkers [9]. Nonetheless, the required repetition of CBD cycles in their process severely impacted the device fabrication time.

Aside from the aforementioned solution-based processes, Several vacuum-based techniques for depositing SnO_2 thin films have also been considered and could show promising results as well [15–19]. Among them, Atomic Layer Deposition (ALD) seems particularly attractive thanks to its ability to grow dense and homogeneous thin films with an ultimately fine control over film thickness at moderate temperatures [20–23]. Beyond this, ALD allows for ultra-conformal deposition on top of wide and textured areas [24]. Growing SnO_2 ESL by ALD would be especially adapted to the case of Pvk/crystalline Silicon (c-Si) tandem solar cells. Such devices, which show exciting theoretical efficiency limits above 35% [25,26], require, in their monolithic 2-Terminal (2T) architecture to integrate all Pvk top-cell nm-thick constitutive layers on top of a large-area c-Si bottom-cell textured with μm-high pyramids. Experimental lab scale devices have already reached 32.5% power conversion efficiency [27], thereby overcoming both state-of-the-art c-Si solar cells efficiency and its theoretical limit of 29.8 % [28] and highlighting how promising the tandem technology is for cheap and efficient sunlight energy conversion into ready-to-use electricity.

Several groups have therefore investigated a SnO_2 ESL fabrication by Atomic Layer Deposition (ALD), and most of them pointed out performance limitations of Pvk-based devices [19,29–32]. The explored causes of observed performance losses are diverse and most of them depend on the solar cell architecture. In studies where an ALD-grown SnO_2 (SnO_2^{ALD}) ESL is deposited on top of the Pvk absorber (the so-called inverted architecture, or P-I-N), the latter may suffer from chemical degradation at Pvk-SnO_2^{ALD} interface [31,33]. Although state-of-art Pvk/c-Si tandem solar cells that integrate SnO_2^{ALD} feature the P-I-N architecture, they typically make use of another material thin film, commonly a fullerene, such as C_{60}, in between Pvk and SnO_2^{ALD} which prevents Pvk degradation during the ALD process [34–37]. In devices where the Pvk absorber film is grown on top of the SnO_2^{ALD} ESL (N-I-P architecture), the layers stack order prevents any Pvk degradation through SnO_2^{ALD} growth. Several works on N-I-P Pvk-based cells also unveiled interfacial limitations, leading to lower cell performance than when using a solution-processed SnO_2 ESL. In that respect, Wang and coworkers, while using a bilayered ESL with the addition of a C60 self-assembled monolayer between SnO_2^{ALD} and Pvk, highlighted that a poor electrical conductivity of the ESL could lead to electrons and holes transportation imbalance, thus enhancing hysteresis effects [29]. Aygüler et al. claimed a strong correlation between N-I-P Pvk-based solar cell performances and the Fermi level alignment between their SnO_2^{ALD} ESL and Pvk [38]. Their results agree with Palmström and co-workers findings in their study on the Pvk-SnO_2^{ALD} interface, which, while mostly focused on P-I-N architecture, also showed SnO_2^{ALD}-based devices in the N-I-P configuration with poor performances possibly arising from non-ideal conduction bands alignment between SnO_2^{ALD} and Pvk [31]. Again, adding another thin film, and most often a fullerene, onto the SnO_2^{ALD} layer to form a bi-layered ESL has proven to passivate such defects [31,39]. Nevertheless, using a monolayer would be preferable to simplify the fabrication process and limit the cost of the device. Furthermore, such a Pvk-C_{60} interface can also be performance-limiting [40]. Hence, getting a better knowledge of SnO_2^{ALD}-induced interfacial limitations when employed as a single-layer ESL appears to be of high interest.

While other studies clarified the role of interfacial limitations in P-I-N Pvk SJ solar cells, which could partially result from a Pvk degradation during the ALD process [31,33], this work focuses on studying SnO_2^{ALD}-induced interfacial limitations in N-I-P Pvk single-junction (SJ) solar cells. The emphasis of this study is put on a thorough investigation of SnO_2^{ALD} ESL and its interface with Pvk, rather than presenting improved solar cell performances with respect to state of the art. To this end, SnO_2^{ALD} thin films are systematically compared to a spin-coated nanoparticle-based SnO_2 (SnO_2^{NP}), acting as a reference. First, SJ Pvk solar cells that integrate each type of SnO_2 as ESL are characterized. Subsequently, SnO_2^{NP} and SnO_2^{ALD} as well as their interface with Pvk are energetically and chemically analyzed in an attempt to link material properties to device performances.

II. EXPERIMENTAL SECTION

II.1 Device Fabrication

Single junction Pvk solar cells were fabricated according to the N-I-P architecture. First, 30 nm-thick SnO_2^{ALD} layers were grown on top of commercial glass/ITO substrates at 150°C from Tetrakisdimethylamino-tin(IV) (TDMASn) and hydrogen peroxide (H_2O_2) as tin precursor and oxidizing reactant respectively. Since no front mask was used during the ALD process, glass/ITO/SnO_2^{ALD} samples were subsequently etched down (on one-third of their area) by laser to prevent any contact between the top electrode and SnO_2^{ALD} (Figure 1.a). 30 to 40 nm-thick SnO_2^{NP} layers were prepared by spin-coating a water-based SnO_2 nanoparticles dispersion on pre-etched glass/ITO substrates just after a 30-minute UV-O_3 treatment. Spin-coated samples underwent annealing at 80°C for 1 minute. The Pvk precursor solution, prepared beforehand, was subsequently spin-coated under N_2 atmosphere on top of the SnO_2 layer to form double-cation Pvk with a $Cs_{0.05}FA_{0.95}Pb(I_{0.83}Br_{0.17})_3$ targeted stoichiometry. The precursor solution is based on diluted lead iodide (PbI_2), lead bromide ($PbBr_2$), cesium iodide (CsI) and formamide iodide (FAI) salts in dimethylformamide and dimethylsulfoxide, for an overall lead concentration of 1.2 %m. It must be noted that glass/ITO/SnO_2^{ALD} substrates require a 30-minute UV-O_3 treatment just before Pvk coating to improve surface wettability. 150µL of chlorobenzene was dropped 5 seconds before the spinning of the Pvk precursors solution ended. Afterwards, films were annealed at 100°C for one hour. Then, Poly(triarylamine) (PTAA) doped with Lithium bis(trifluoromethane sulfonyl)imide (LiTFSI) was spin-coated on top of Pvk to form a 100 nm-thick hole selective layer (HSL) [41]. After a chemical etching of PTAA and Pvk films, as well as, for reference cells, the SnO_2^{NP} layer over the areas devoted to contacts, gold top contact was evaporated. The final device architecture is depicted in Figure 1.b.

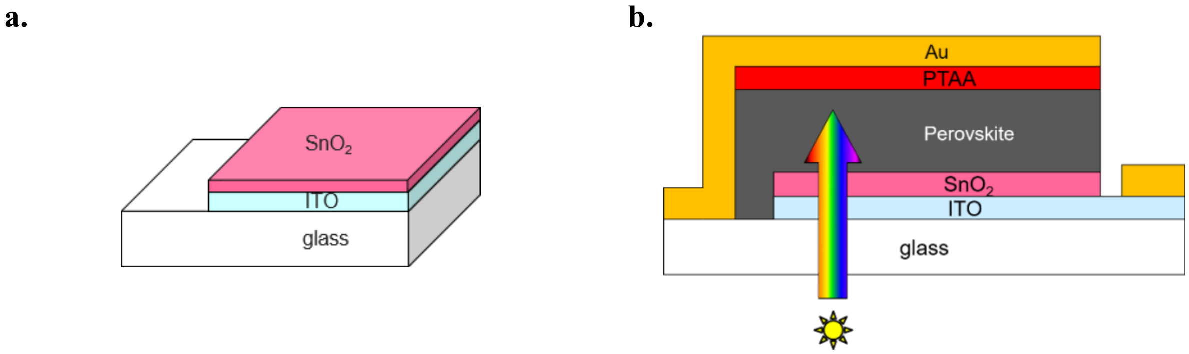

Figure 1. Schematic of a glass/ITO/SnO_2^{ALD} stack just after laser scribing (a.) and of a Pvk solar cell in the N-I-P configuration (b.)

II.2 Characterization Methods

ALD-grown layers stoichiometry was systematically analyzed through Hard X-ray Photoelectron Spectroscopy (HAXPES) with a Cr-Kα X-ray source on a PHI Quantes XPS/HAXPES tool, on glass/SnO_2 and glass/ITO/SnO_2 test samples. SnO_2^{ALD} layers thicknesses were checked by ellipsometry with a UVisuel tool from Horiba Jobin-Yvon. Optical transmission was measured with a Perkin-Elmer UV-visible-nIR spectrophotometer on quartz/SnO_2 samples. The electrical sheet resistance of glass/SnO_2 samples was measured by 4-point probe method on a Napson tool. Hall effect measurements were carried out with an Ecopia instrument from Bridge Technology on glass/SnO_2^{ALD} samples (with and without UV-O_3 treatment) but could not be performed on SnO_2^{NP} layers which were too resistive. Current density – voltage (J-V) analysis was performed on cells in ambient air under calibrated 1 sun illumination.

UV Photoelectron Spectroscopy (UPS) characterization of c-Si/ITO/SnO_2 and c-Si/ITO/SnO_2/Pvk samples was performed using the He I line (eV) of an Escalab 250 Xi tool from ThermoFisher Scientific. For these characterizations, c-Si substrates were chosen to avoid charging effects observed with glass substrates. The Fermi level in all SnO_2 spectra was calibrated on gold Fermi level. Device cross-section images were recorded by Transmission Electron Microscopy (TEM) with a TEM Tecnai Osiris instrument at an acceleration voltage of 200 keV. Time of Flight Secondary Ions Mass Spectroscopy (ToF-SIMS) profiling was also performed on glass/ITO/SnO_2/Pvk stacks with a TOF.SIMS 5 instrument from IONTOF equipped with a Cs^+

monoatomic ion gun for etching and a Bi_3^+ multi-atomic ion gun for analysis. Buried SnO_2/Pvk interface characterization was realized on glass/ITO/SnO_2/Pvk samples by HAXPES with PHI Quantes XPS/HAXPES tool combined with an Ar^+ ion gun for etching. Ar^+ ion etching under 1 kV acceleration voltage was first carried out for 5 minutes to remove most of the Pvk film thickness. Subsequently, a sequence comprising HAXPES measurement followed by 1 minute of ion etching was cycled three times to characterize the SnO_2/Pvk buried interface.

III. RESULTS AND DISCUSSION

III.1 Performance limitations induced by ALD-grown SnO_2 ESL

Before getting integrated into Pvk-based solar cells, ALD-grown film chemical, optical and electrical properties were first checked by HAXPES, spectrophotometry and resistivity measurements, respectively. These characterization results can be compared to the ones of reference SnO_2^{NP} in Table 1. First, according to a quantitative analysis of HAXPES measurements, both SnO_2^{NP} and SnO_2^{ALD} layers show an overall oxygen O to tin Sn ratio ([O]/[Sn]) larger than 2. However, the O 1s peak features two contributions to the overall HAXPES signal for both types of SnO_2, as visible in Figure S1 (see Supplementary Information). This extra contribution, which rises as a clear shoulder at high binding energy ($E_B \approx 531.4 \pm 0.5$ eV) next to the main contribution ($E_B \approx 530.1 \pm 0.5$ eV), is attributed to –OH related species [30,32,42–44]. Therefore, as shown in Table 1, the ratio of O elements that are chemically involved in metallic bonds with Sn over the total Sn concentration in these films appears to be smaller than 2. Hence, both types of films seem to contain a major SnO_x phase, with $1.8 \leq x < 2$, which is slightly under-stoichiometric, mixed with oxidized compounds such as –OH species. This result is quite common for SnO_2 thin films deposited at low temperatures [43,45] and these oxygen vacancies are believed to be the origin of the native N-type doping and thus of the electrical conductivity in SnO_2 [6,21,46].

Table 1. Ratios of total and partial O concentration over Sn concentration, averaged electrical resistivity and effective optical transmission of SnO_2^{NP} and SnO_2^{ALD} 30 nm-thick films deposited on glass (or quartz substrates for transmission measurements).

	[O]/[Sn]	**[O_{Sn}]/[Sn]**	**Electrical resistivity [Ω.cm]**	**Effective optical transmission [%] (300 - 1100 nm)**
SnO_2^{NP}	2.4 ± 0.1	1.9 ± 0.1	$(2.3 \pm 0.2) \times 10^{2}$	92 ± 1
SnO_2^{ALD}	2.1 ± 0.1	1.8 ± 0.1	$(6.1 \pm 0.4) \times 10^{-3}$	88 ± 1

On this aspect, the slightly lower amount of O in SnO_2^{ALD} films in comparison to SnO_2^{NP} films agrees with the strongly reduced electrical resistivity of the former with respect to the reference films. The large electrical resistivity difference (by a factor close to 40,000) between these two types of films may also be explained by the nanoparticular nature of SnO_2^{NP} in which current flow is probably hindered at each nanoparticle boundary. Thanks to its low resistivity, integrating a 30 nm- thick SnO_2^{ALD} layer should not limit electron transport throughout the device.

Furthermore, from Table 1, one can see that the effective optical transmission of quartz/SnO_2^{ALD} stacks over the 300-1,100 nm range remains close to that of quartz/SnO_2^{NP} samples. The small reduction arises mainly from short wavelengths as illustrated by transmission spectra in Figure S2 (see Supplementary Information). Hence, using a SnO_2^{ALD} ESL may have a negative impact on current generation in a N-I-P SJ Pvk solar cell, for which sunlight goes through the ESL to reach the Pvk film. On the contrary, it should not limit optically the performances in N-I-P tandem Pvk/c-Si solar cells, for which sunlight impinges the Pvk film through the HSL side.

Therefore, except for an eventual optical limitation, all characterized properties seem adequate for the use of a SnO_2^{ALD} thin film as an ESL in Pvk-based SJ solar cells. However, it appears on the J-V curves presented in Figure 2, how integrating such SnO_2^{ALD} ESL induces strong performance limitations of SJ Pvk solar cells, in agreement with previous reports [30,31]. All photovoltaic operation parameters are affected (see Table S2 in Supplementary Information) which reduces the power conversion efficiency of SnO_2^{ALD}-based cells to around 7.5 %, on average over several tens of cells. In comparison, the averaged power conversion efficiency measured over several tens of reference SnO_2^{NP}-based cells is more than twice larger (see Table S2). A slope-breaking, observed in Figure 2 within the 0.5 – 1.2 V region, causes a strong Fill Factor (FF) and open-circuit-voltage (V_{OC}) reduction. It may be the signature of inadequate energy bands alignment which could involve an electron barrier at the SnO_2^{ALD}/Pvk interface [47]. Besides, the slope visible on the J-V curve related to the SnO_2^{ALD}-based cell at small positive voltages indicates a higher shunt current than for the reference cell. Additionally, the very weak reverse breakdown voltage noted for SnO_2^{ALD}-based cells underlines a poor hole-blocking ability compared to SnO_2^{NP}. Finally, J-V curves recorded in a forward scan highlight how the hysteresis increases upon using SnO_2^{ALD} rather than SnO_2^{NP}. All these phenomena seem to point out a lack of charge selectivity as well as a probable limited electron extraction from Pvk to SnO_2^{ALD} [47–50].

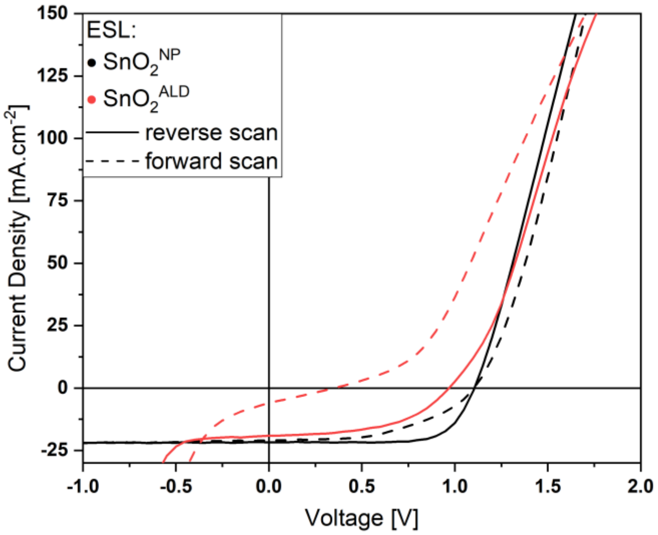

Figure 2. J-V curves of Pvk cells that integrate a reference SnO_2^{NP} ESL or a SnO_2^{ALD} ESL recorded under 1 sun illumination.

III.2 Investigation of the SnO_2/Perovskite electrical junction

III.2.1 Workfunction and valence band maximum characterization

The analysis of SnO_2^{ALD}-based Pvk cells behavior suggests an energy potential barrier at the conduction band junction between SnO_2^{ALD} and Pvk which would hinder electron extraction [50]. The knowledge of SnO_2^{ALD} and Pvk respective workfunctions and electronic affinities can help to validate this hypothesis. Regarding the characterization of the former property, UPS has been performed on c-Si/ITO/SnO_2 and of c-Si/ITO/SnO_2/Pvk samples for both types of SnO_2. Corresponding spectra are visible in Figure 3.

From the electron cut-off region in Figure 3.a, SnO_2^{ALD} and SnO_2^{NP} workfunction values can be determined thanks to the relation $\phi = h\nu - E_{\mathrm{cutoff}}$. A significantly larger workfunction is found for SnO_2^{ALD} layers than for reference SnO_2^{NP} films with $\phi^{\mathrm{ALD}} \approx 4.77$ eV and $\phi^{\mathrm{NP}} \approx 4.22$ eV, respectively. The characterized workfunction for SnO_2^{ALD} also appears to be relatively high with respect to common values found in literature, which are about few hundreds meV lower [32,38,51,52]. Although it may appear counter-intuitive given the above reported conductivity and O to Sn concentration ratios for SnO_2^{ALD} and SnO_2^{NP}, the fact that an increase in workfunction in a N-type semiconductor is not linked to reduced doping can be explained by a non-negligeable difference in bandgap energies between these two materials and in particular to a larger electron affinity, which is also linked to the doping level, eventual semiconductor degeneracy, and surface impurities [53, 54]. A linear approximation of the spectra at the electron signal onset in Figure 3.a allows the determination of the valence band maximum energy level E_V with respect to the Fermi level. Again, different values are obtained, with $E_V^{\mathrm{ALD}} \approx 3.52$ eV and $E_V^{\mathrm{NP}} \approx 4.27$ eV for SnO_2^{ALD} and SnO_2^{NP}, respectively.

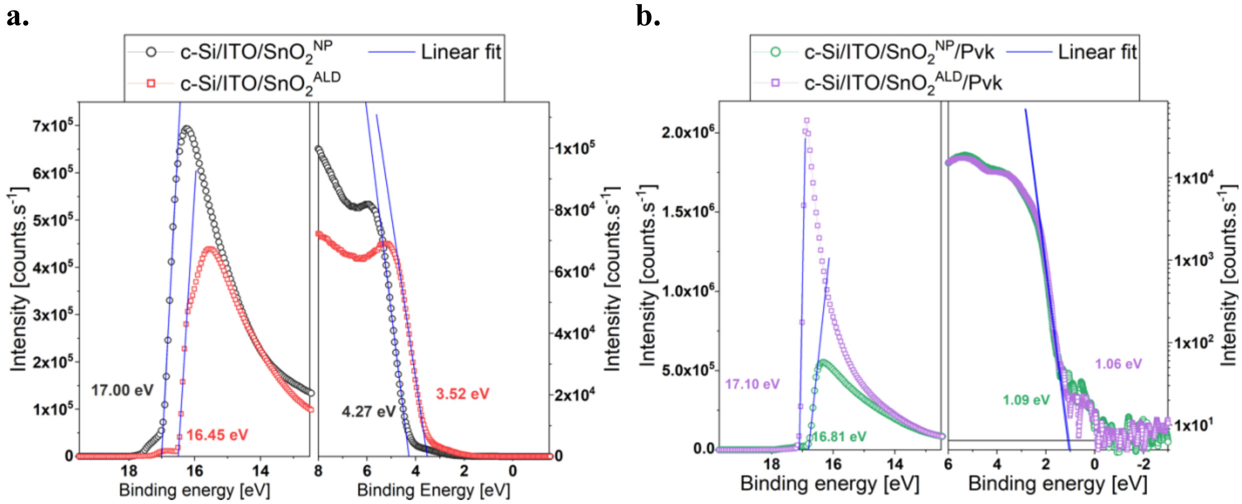

Figure 3. UPS spectra obtained on c-Si/SnO_2^{ALD} or c-Si/SnO_2^{NP} samples (a.) and c-Si/ SnO_2^{ALD}/Pvk and c-Si/ SnO_2^{NP}/Pvk samples (b.), focused on their respective electron cut-off and valence band signal onset regions. All spectra have their Fermi energy level at $E = 0$ eV calibrated on the one of gold.

Similarly, from the electron cut-off region in Figure 3.b, one can extract the Pvk workfunction. As reported in several studies where Pvk workfunction is influenced by its underlying substrate [19,55-58], it appears to be different according to the underlying SnO_2 layer. In this work, a value of $\phi^{\mathrm{Pvk,ALD}} \approx 4.12$ eV or $\phi^{\mathrm{Pvk,NP}} \approx 4.41$ eV is found for Pvk deposited on top of SnO_2^{ALD} or SnO_2^{NP} respectively. The fact that the workfunction measured at the very surface of Pvk films is dependent on the substrate they rely on may be linked to their low doping density [57, 58]. From the valence band onset in Figure 3.b, plotted in a semi-logarithm scale according to the technique used by Schulz et al. [55,58], a similar valence band maximum has been found for both Pvk films, with a value of $E_{\mathrm{V}}^{\mathrm{Pvk,ALD}} \approx 1.06$ eV and $E_{\mathrm{V}}^{\mathrm{Pvk,NP}} \approx 1.09$ eV respectively. Comparing these results to the optical bandgap energy $E_g^{\mathrm{opt}} \approx 1.6$ eV determined for these films from spectrophotometry measurements (see Figure S4, in Supplementary Information), it appears that Pvk films have a slight N-type doping, which is in agreement with the excess of lead iodide (PbI_2) implied in films fabrication [59].

One can also notice in Figure 3.b a slope in the photoelectron signal starting from the middle of the gap, before the valence band onset. Such observation may be the signature of mid-gap trap states in the Pvk [60]. The presence of such deep trap states within the Pvk bandgap should in principle induce non-radiative recombination in Pvk-based solar cells. However, as UPS is a technique with a very shallow probing depth (~1–3 nm), such defect states could also be only present at the Pvk film surface while being absent in the bulk [55].

III.2.2 SnO_2/Pvk electrical junction investigation

UPS results show a strong difference between SnO_2^{ALD}/Pvk and SnO_2^{NP}/Pvk interfaces. There is a significant increase in workfunction in the device stack when going from Pvk to SnO_2^{ALD}

whereas a decrease in workfunction is observed in the reference case when going from Pvk to SnO_2^{NP}. In order to confirm if this difference causes an energy barrier at the SnO_2^{ALD}/Pvk interface, it is helpful to build a picture of the SnO_2/Pvk electrical junction, which requires the knowledge of the conduction band minimum energy level, E_C. Although no direct measurement could have been performed (for instance by Inverse Photoelectron Spectroscopy, IPES, [55]), E_C with respect to the vacuum level, that is the electron affinity χ, can be calculated from the knowledge of the workfunction ϕ and E_V providing one also knows the bandgap energy E_g from the relation: $\chi = \phi + E_V - E_g$.

The bandgap of our Pvk films grown on top of both types of SnO_2 has been deduced from spectrophotometry measurements (see Figure S4) and it was found to be $E_g^{opt} \approx 1.6 \pm 0.1$ eV.

To investigate SnO_2^{NP} and SnO_2^{ALD} bandgap energies, their respective absorption coefficient spectra $\alpha(h\nu)$, visible in Figure S3, have been extracted from extinction coefficient (κ) obtained by ellipsometry measurements on c-Si/SnO_2 samples through the relation: $\alpha = \frac{4\pi}{\lambda}\kappa$. SnO_2 has been mainly reported to be a direct bandgap semiconductor in literature [53, 61–63]. Its optical bandgap (E_g^{opt}) can be estimated by the well-known Tauc method, consisting in plotting $(\alpha h\nu)^2$ as a function of photon energy $h\nu$ [64]. As one can see from the Tauc plot in Figure 4, an estimation of $E_g^{opt} = 3.7 \pm 0.1$ eV is found for SnO_2^{ALD}, and of $E_g^{opt} \approx 4.4 \pm 0.1$ eV for SnO_2^{NP}. These values fall within the range of bandgap energies found in literature for SnO_2 [5,7,43,46,63]. The significantly larger value for SnO_2^{NP} could arise from a quantum confinement effect in nanoscale crystalline grains as suggested by Mullings et al. [22], considering the nanoparticle-based nature of the SnO_2^{NP} thin films (for which nanoparticles diameter can be smaller than 5 nm while the size of embedded crystallite could be even smaller).

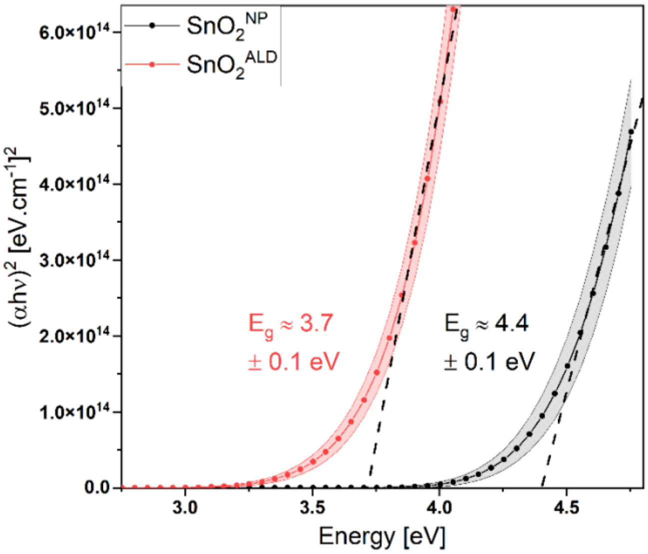

Figure 4. Tauc representations of SnO$_2^{NP}$ and SnO$_2^{ALD}$ absorption coefficient for direct bandgap materials.

A hypothetical energy diagram can be drawn from these optical bandgap estimates and UPS characterization results, assuming that the electrical bandgap and the optical bandgap are the same, as represented in Figure 5 for SnO$_2^{NP}$ and SnO$_2^{ALD}$, respectively. From Figure 5.a and Table 2, a difference of $E_C - E_F = \phi - \chi \approx 0.13$ eV is observed between the conduction band minimum and the Fermi energy level of SnO$_2^{NP}$. This experimental value appears too low when considering the electrical resistivity presented in Table 1. As a matter of fact, assuming a carrier mobility μ = 100 cm^2 V^{-1} s^{-1} [6,44] and an effective density of the conduction band $N_c \approx 3.5 \times 10^{18}$ cm^{-3} [65], one deduces from the resistivity an estimate of $E_C - E_F$ of 0.2 eV. However, due to its nanoparticle-based nature, SnO$_2^{NP}$ may see its thin film electrical resistivity enlarged at each particle boundaries, probably leading to an overestimated computed $E_C - E_F$. Hence, given experimental errors in the measured values of ϕ and E_g^{opt} and uncertainties in the values of μ and N_C, the energy diagram presented in figure 5.a can still be considered as valid to be compared with the one of Pvk (Figure S5, in Supplementary Information).

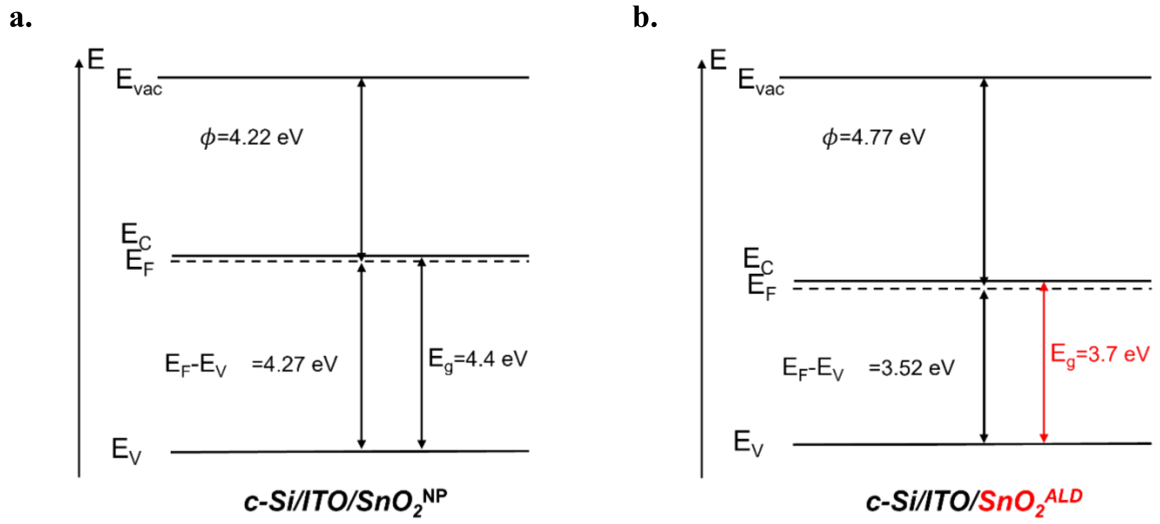

Figure 5. Energy diagram of SnO_2^{NP} (a.) and SnO_2^{ALD} (b.) built from UPS characterization results and the estimate of the optical bandgap by the Tauc method assuming a direct bandgap.

In the case of SnO_2^{ALD}, it can be observed from Figure 5.b that $E_C - E_F$ calculated from the extracted optical bandgap is approximatively 0.18 eV. This appears inconsistent with the low electrical resistivity value measured for SnO_2^{ALD} films (see Table 1) which is associated with a large electron concentration of $1.5 \pm 0.2 \times 10^{20}$ cm^{-3}, as measured by Hall effect (see Table S1 in Supplementary Information), which rather points toward a degenerate semiconductor.

Indeed, a degenerate SnO_2 may present an optical bandgap energy value that is different from the electronic energy bandgap at the center of the Brillouin zone due to the Burstein-Moss effect [66,67]. This phenomenon is known to increase the measured optical bandgap of highly doped and degenerate semiconductors with respect to the electronic bandgap due to the partial fillings of conduction band energy states while shifting the Fermi wavevector, k_F, off the center of the Brillouin zone (i.e $k_F \neq 0$) [66,67]. Here, the Burstein-Moss widening effect is calculated to be as large as $\Delta E_{BM} \approx 0.3$ eV (see Supplementary Information). Consequently, the value of the conduction band minimum position $E_C - E_F \approx 0.18$ eV computed in Figure 5 assuming $E_g^{opt} =$

$E_C - E_V$ is also largely overestimated and is believed to rather be negative to express SnO_2^{ALD} thin films degenerate character.

Table 2. Measured workfunction ϕ, valence band maximum E_{VBM} and optical energy bandgap E_g^{opt} and calculated electron affinity χ of SnO_2^{NP} layers, of Pvk films deposited on SnO_2^{NP}, of SnO_2^{ALD} layers and of Pvk films deposited on SnO_2^{ALD}.

	ϕ [eV]	E_{VBM} [eV]	E_g^{opt} [eV]	χ [eV]
SnO_2^{NP}	4.22 ± 0.02	4.27 ± 0.05	4.4 ± 0.1	4.1 ± 0.1
SnO_2^{NP}/Pvk	4.41 ± 0.02	1.09 ± 0.05	1.6 ± 0.1	3.9 ± 0.1
SnO_2^{ALD}	4.77 ± 0.02	3.52 ± 0.05	3.7 ± 0.1	//
SnO_2^{ALD}/Pvk	4.12 ± 0.02	1.06 ± 0.05	1.6 ± 0.1	3.6 ± 0.1

Now comparing energy diagrams for SnO_2^{NP} in Figure 5.a and Pvk in Figure S5.a (see Supplementary Information) and quantities in Table 2, one can see that SnO_2^{NP} electron affinity is larger than that of Pvk deposited on top of such SnO_2^{NP}. At the same time, SnO_2^{NP} workfunction is smaller than for Pvk. Consequently, as illustrated by junction energy diagrams schematized in Figure 6.a, the electrical junction at SnO_2^{NP}/Pvk interface is expected to be electron selective and not limiting for electron transport, in agreement with SnO_2^{NP}-based Pvk cells performances.

On the contrary, if SnO_2^{ALD} is degenerate, no electron affinity value can be determined. Furthermore, SnO_2^{ALD} workfunction is much larger than that of Pvk (see Table 2 and Figures 5.b and S5.b in Supplementary Information). As illustrated in Figure 6.b, this situation gives rise to an energy barrier at the SnO_2^{ALD}/Pvk interface.

Such energy barrier, which does not exist for the reference SnO_2^{NP} (see Figure 6.a), may strongly hinder electron extraction out of the Pvk and could explain the slope-breaking observed in J-V curves of SnO_2^{ALD}-based cells (Figure 2), as hypothesized in section III.1 [47,50]. Furthermore, the band bending at the SnO_2^{ALD}/Pvk interface pictured in Figure 6.b may also promote non-radiative interfacial recombination mechanisms. Holes accumulation in Pvk valence band at the interface with SnO_2^{ALD} would increase the non-radiative recombination probability via a direct tunneling of holes from the Pvk valence band to occupied states below the Fermi level in SnO_2^{ALD} (Figure 6.b). [48,50]. As schematized in Figure 6.b, the possible presence of interfacial trap states could further enhance the non-radiative recombination probability. Such phenomenon would thus explain the high non-radiative recombination rate assumed from J-V curves analysis in section III.1 and could be at the origin of the characterized low selectivity of SnO_2^{ALD}.

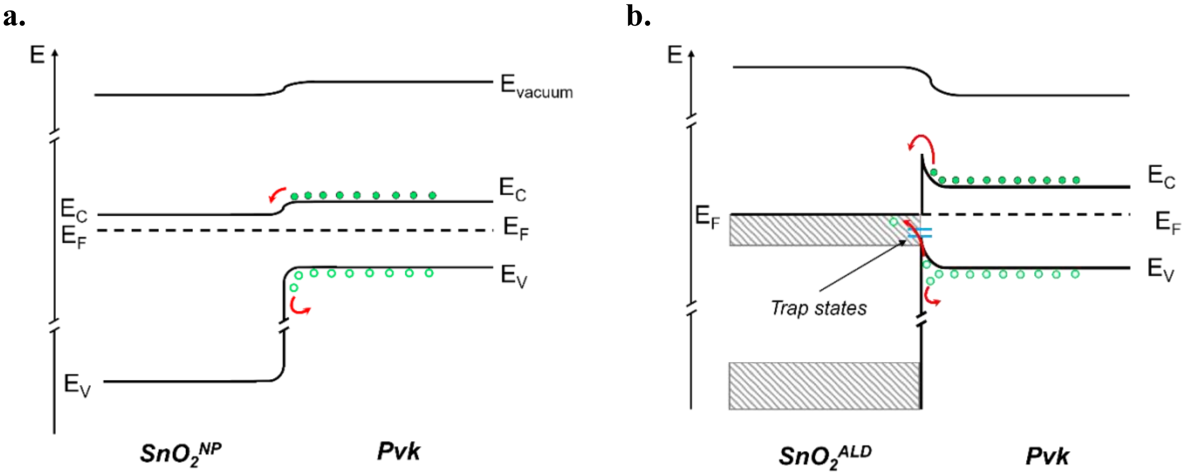

Figure 6. Schematic energy diagrams of the SnO_2^{NP}/Pvk electric junction (a.) and of the SnO_2^{ALD}/Pvk electric junction (b.) built according to Anderson rule.

III.3 SnO_2/Perovskite interface chemical analysis

III.3.1 ToF-SIMS profiling

As already mentioned, UPS is a very sensitive technique that can only probe a very shallow depth (~1-5 nm) below a material surface [55]. Therefore, a chemical analysis of the SnO_2^{ALD} thin film surface may help to understand UPS characterization results just described and could also give further insight into the cause of the suspected high non-radiative recombination velocity. From TEM cross-section images in Figures 7.a and 7.b, one can see that in both cases, the SnO_2 layer seems homogeneous and pinhole-free, which should prevent any direct contact between the ITO and Pvk thin films.

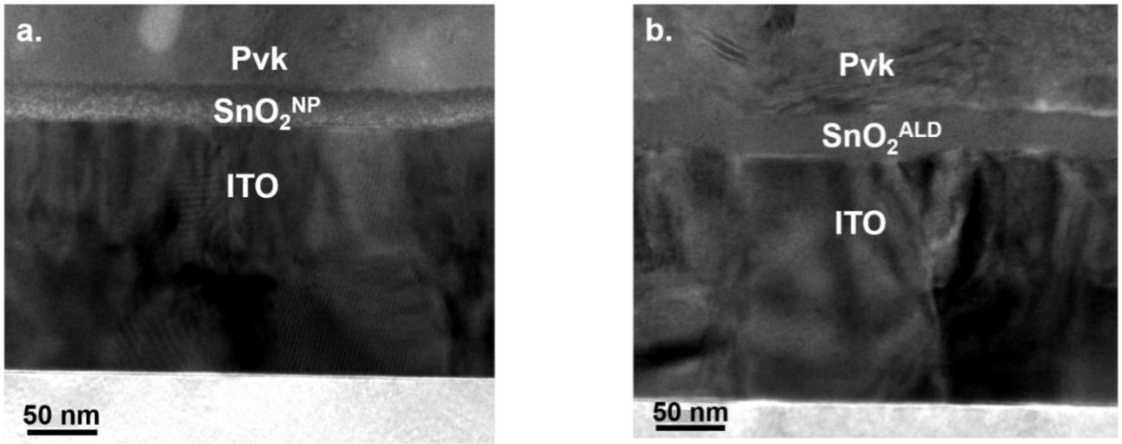

Figure 7. TEM cross-section image of a c-Si/ITO/SnO_2^{NP}/Pvk stack (a.) and a c-Si/ITO/SnO_2^{ALD}/Pvk stack (b.).

Interestingly, ToF-SIMS depth profiling on glass/ITO/SnO_2^{ALD}/Pvk and glass/ITO/SnO_2^{NP}/Pvk samples showed a different chemical structure between these two stacks. Normalized ToF-SIMS intensity depth profiles are plotted in Figure 8 as a function of etching time. It is useful to highlight here that such normalized representation in a linear scale is not common in ToF-SIMS analysis. ToF-SIMS profiles are mostly plotted on a semi-logarithm scale in literature [68,69], such as in Figure S6 (see supporting information). Nevertheless, superimposing in a single plot numerous profiles relative to different ionic fragments, like in Figure S6, makes the analysis of the results uneasy. Besides, since matrix effects prevent any direct link between signal intensity for a specific fragment and its concentration in the probed layer, comparing the respective intensity of various fragments is even more unworkable. However, intensity slope variations hold the information relative to the evolution of a fragment concentration along the depth profile. Therefore, in order to visualize these variations for all analyzed ionic fragments in a single plot, the intensity profiles in Figure S6 have been represented on a linear scale normalized between 0 and 1 in Figure 8.

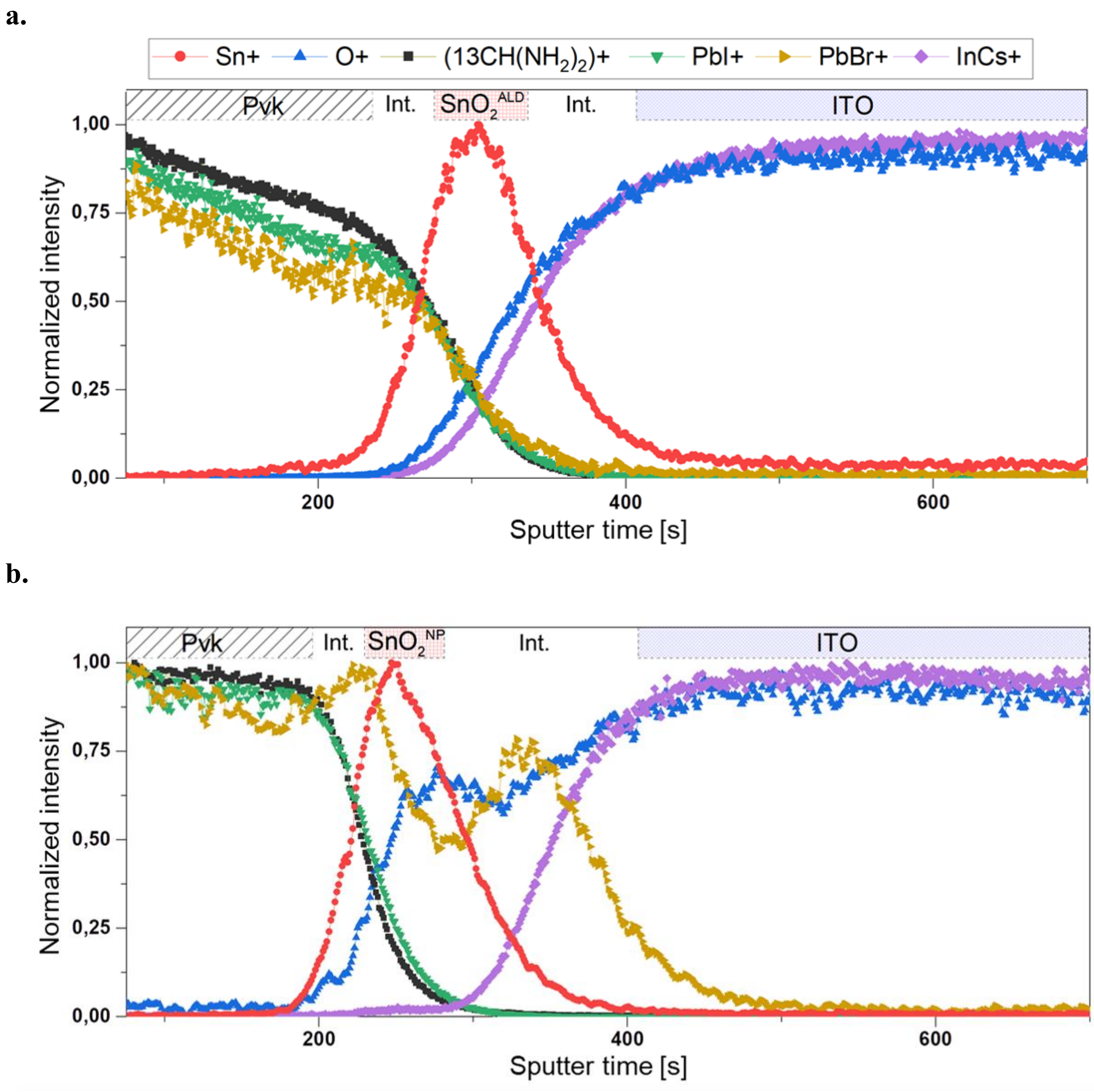

Figure 8. ToF-SIMS normalized intensity profiles of a selection of ionic fragments extracted from a glass/ITO/SnO_2^{ALD}/Pvk stack (a.) and a glass/ITO/SnO_2^{NP}/Pvk stack (b.). The "Int." abbreviation stands for interface.

Looking at Figure 8.a, a first decreasing slope is noted for Pvk-related fragments ($(13CH(NH_2)_2)^+$, PbI^+, $PbBr^+$) within the bulk of Pvk film (before the Sn^+ signal onset) deposited on top of glass/ITO/SnO_2^{ALD} whereas the intensity of the same fragments remains stable in Pvk films grown on glass/ITO/SnO_2^{NP} in Figure 8.b. Although this decreasing slope may be linked to a measurement artifact [69], its absence in the reference stack case would more likely point out different distributions of elements that compose Pvk films depending on the underlying SnO_2.

According to the different fragments profile variations along the etching depth, one can see in Figure 8.a that no Pvk-related elements seem to penetrate within the SnO_2^{ALD} layer. However, a significant delay between the Sn^+ and O^+ signal onsets can be noticed, and O^+ intensity variations are more in phase with the ones of $InCs^+$ fragments. This trend indicates an important lack of oxygen in the SnO_2^{ALD} layer top-half or at least at the interface with the Pvk film. This result is quite surprising according to HAXPES characterizations on bare SnO_2^{ALD} layers (see section III.1). Matrix effects in Tof-SIMS intensity of each chemical environment (Pvk, SnO_2^{ALD} then ITO) and at each change in chemical environment (Pvk to SnO_2^{ALD} and SnO_2^{ALD} to ITO) associated to the relatively small thickness of the SnO_2^{ALD} layer may interfere here with the O^+ signal. Nevertheless, it can be seen in Figure 8.b that no lack of oxygen is detected with the SnO_2^{NP} layer, and the O^+ signal onset rises at a similar time as the Sn^+ signal. However, in Figure 8.b, a significant decoupling is observed between the intensity profiles related to the $(13CH(NH_2)_2)^+$ and PbI^+ fragments with respect to the profile of $PbBr^+$ fragments at the SnO_2^{NP}/Pvk interface. While there is a strong decrease in signal intensity for $(13CH(NH_2)_2)^+$ and PbI^+ fragments signal, the $PbBr^+$ related signal increases at the interface with SnO_2^{NP}. Furthermore, after a decay within the SnO_2^{NP} layer, the $PbBr^+$ signal rises again at the ITO/SnO_2^{NP} interface. These observations show an accumulation of a certain –PbBr-rich phase at SnO_2^{NP}/Pvk and ITO/SnO_2^{NP} interfaces. The decaying but relatively high $PbBr^+$ signal intensity within the SnO_2^{NP} agrees with the penetration of a –PbBr-based phase through the layer. No similar observation can be made when looking at Figure 8.a, which does not show the penetration of any Pvk-related fragment through the SnO_2^{ALD} layer.

III.3.2 Buried interface analysis

Thanks to its specific probing depth (~10-20 nm [55]), HAXPES characterization of the SnO_2/Pvk interface has been performed on glass/ITO/SnO_2^{NP}/Pvk and glass/ITO/SnO_2^{ALD}/Pvk stacks, after having etched Pvk films down to a very low thickness allowing to see a signal from Sn 2p, O 1s, Pb 4f, I 3d orbitals simultaneously (see section II.2). Figure 9 shows the fitted O 1s orbital spectra after 7 minutes and 8 minutes of Ar^+ ion etching on glass/ITO/SnO_2^{NP}/Pvk and glass/ITO/SnO_2^{ALD}/Pvk samples. First, contrary to the case of reference, after 7 minutes of Ar^+ ion etching, the O 1s signal is hardly distinguished from background noise in the case of a SnO_2^{ALD}-based stack. After an additional minute of ion etching, the photo-electron signal from O 1s orbital is detected for both types of stacks. Peak fitting unveils several contributions to the overall signal in both cases. The main contribution, rising for a binding energy of $E_B \approx 530.4 \pm 0.5$ eV corresponds most likely to O atoms that are involved in covalent bonds with Sn [70]. The contribution shouldering the main peak at high binding energies is probably related to hydrogenated species, such as hydroxyl groups [30,32,42,44]. The third contribution that rises at lower binding energies than that of Sn-O chemical bonds is more complex to identify. Although this could not have been confirmed through the analysis of the Pb 3d HAXPES signal (which was too impacted by the Ar^+ ion etching), it may correspond to another metal oxide [71,72], such as a lead oxide like PbO or PbO_2 [73].

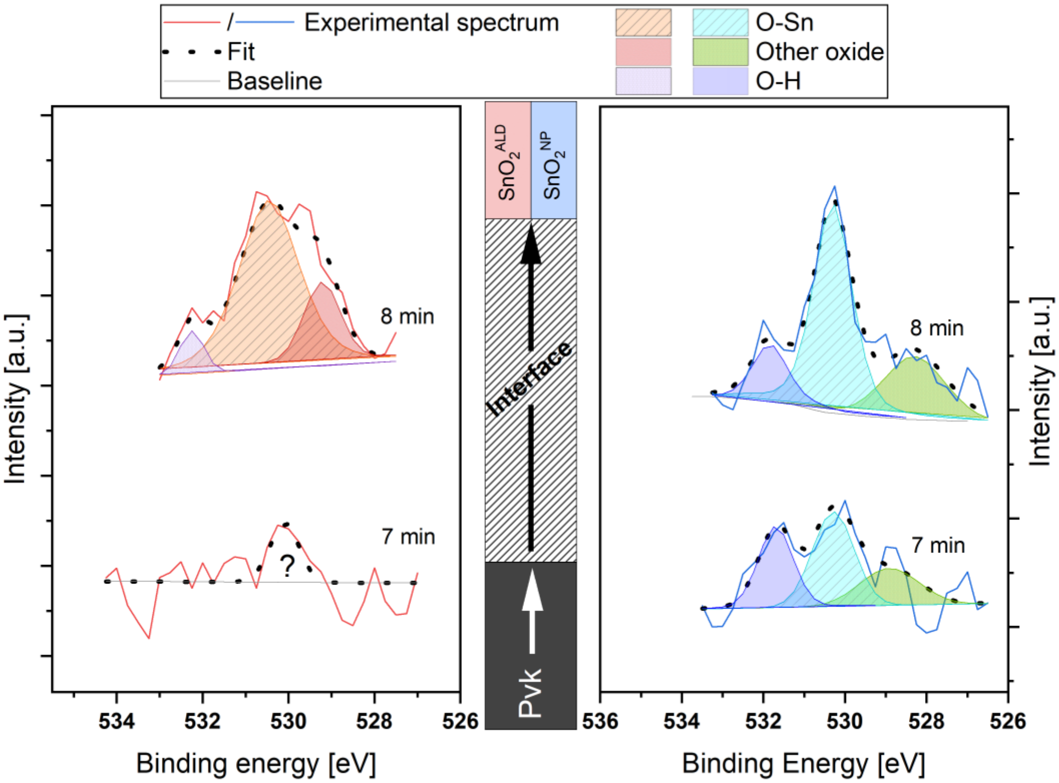

Figure 9. O 1s HAXPES spectra after 7 and 8 minutes of Ar^+ etching on glass/ITO/SnO_2^{ALD}/Pvk (left) and glass/ITO/SnO_2^{NP}/Pvk (right) stacks.

Looking at Sn $2p_{3/2}$ orbital spectra in Figure 10 of the same glass/ITO/SnO_2^{NP}/Pvk and glass/ITO/SnO_2^{ALD}/Pvk samples, it appears that Sn atoms signal is detected in both cases after only 7 minutes of etching. Relatively to the non-simultaneous rise of O 1s signal in Figure 9, this corroborates the lack of oxygen at the SnO_2^{ALD}/Pvk interface revealed by ToF-SIMS (Figure 8). Besides, contrary to the SnO_2^{NP}-based stack, the fitted signal of SnO_2^{ALD}-based samples is composed of different contributions. After 7 minutes of etching, a contribution at lower binding energies is visible next to the main contribution which arises around $E_B \approx 3{,}930.5 \pm 0.5$ eV. According to literature, this secondary contribution probably testifies to the presence of metallic Sn^0 at the SnO_2^{ALD}/Pvk interface, in agreement with a lack of oxygen in this region. An unexpected third contribution to Sn $2p_{3/2}$ overall signal rises after 8 minutes of etching is also noted in Figure 10. As tin oxides (and among them SnO_2) induce the highest binding energies for Sn orbitals electrons [74], an eventual artefact effect from measurement or fitting cannot be excluded.

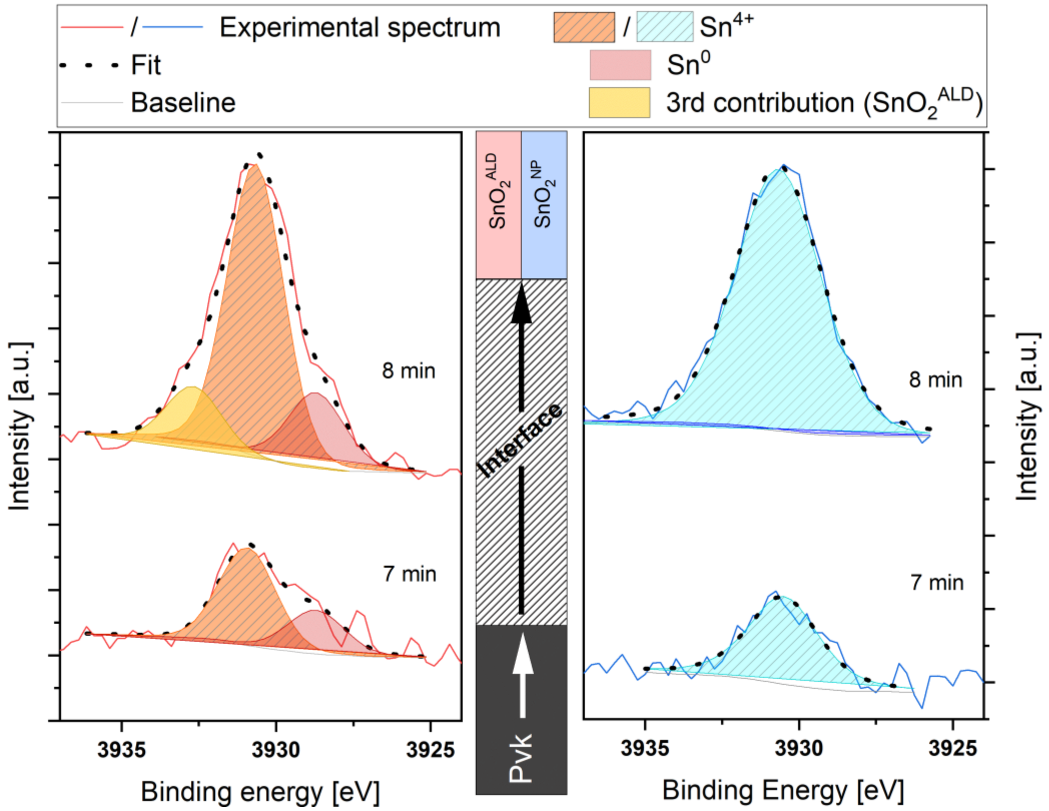

Figure 10. Sn $2p_{3/2}$ HAXPES spectra after 7 and 8 minutes of Ar^+ etching on glass/ITO/SnO_2^{ALD}/Pvk (left) and glass/ITO/SnO_2^{NP}/Pvk (right) stacks.

IV. CONCLUSION

In view of performance limitations induced by the use of a SnO_2^{ALD} ESL in Pvk solar cells, this comparative study focused on the analysis of the SnO_2/Pvk interface. UPS characterization of SnO_2^{ALD} layers and Pvk thin films deposited on SnO_2^{ALD} unveiled an unfavorable band bending at SnO_2^{ALD}/Pvk interface. First, and contrary to reference SnO_2^{NP}/Pvk interfaces, the presence of an energy barrier at the interface between Pvk and SnO_2^{ALD} conduction bands was confirmed, as expected from J-V analysis of SnO_2^{ALD}-based Pvk cells. Besides, it is believed that the band bending at SnO_2^{ALD}/Pvk interface may promote non-radiative recombination of carriers, thereby strongly limiting SnO_2^{ALD} selectivity.

Such poor selectivity may be linked to a surprising lack of oxygen at the SnO_2^{ALD}/Pvk interface, as first suggested by ToF-SIMS characterizations and confirmed through an analysis of the buried SnO_2^{ALD}/Pvk interface by HAXPES. This result, in contrast to the excess of O species found by HAXPES characterization on bare SnO_2^{ALD}, asks the question of an eventual interface modification by device fabrication process. Examining if SnO_2^{ALD} chemical nature could be modified by Pvk deposition may give rise to interesting findings and help in pushing further the interpretation of the obtained results in this study.

Besides, ToF-SIMS characterizations have also unveiled that a phase composed of –PbBr species penetrates the SnO_2^{NP} whereas the SnO_2^{ALD} layer, being denser, appears impermeable to any Pvk-related compound. This PbBr-based phase seems to accumulate at the SnO_2^{NP}/Pvk interface as well as the ITO/SnO_2^{NP} interface. Such phenomenon does not generate significant performance degradation, as visible from reference cells J-V curves in section III.1. However, further investigation would be needed to understand the consequences of the penetration and accumulation of these –PbBr compounds on Pvk-based solar cells behavior. On that matter, studying the hypothesis of an eventual passivating effect granted by the –PbBr phase may lead to useful insight.

ACKNOWLEDGMENT

Part of this work, carried out on the Platform for Nano-characterisation (PFNC) of the CEA Grenoble research center, was supported by the "Recherches Technologiques de Base" program of the French National Research Agency (ANR).

ASSOCIATED CONTENT

Additional contents concerning SnO_2 thin films characterization, Pvk films characterization and SnO_2/Pvk analysis can be found in a separate file. Available free of charge.

AUTHOR INFORMATION

Corresponding Author

* Félix Gayot, felix.gayot@protonmail.com

Author Contributions

All authors have approved the final version of the manuscript.

Notes

The authors declare no competing financial interest.

REFERENCES

[1] J.Y. Kim, J.-W. Lee, H.S. Jung, H. Shin, N.-G. Park, High-Efficiency Perovskite Solar Cells, Chem. Rev. 120 (2020) 7867–7918. https://doi.org/10.1021/acs.chemrev.0c00107.

[2] W. Tress, Perovskite Solar Cells on the Way to Their Radiative Efficiency Limit – Insights Into a Success Story of High Open-Circuit Voltage and Low Recombination, Advanced Energy Materials. 7 (2017) 1602358. https://doi.org/10.1002/aenm.201602358.

[3] F. Zu, D. Shin, N. Koch, Electronic properties of metal halide perovskites and their interfaces: the basics, Mater. Horiz. (2021). https://doi.org/10.1039/D1MH01106E.

[4] M.A. Green, E.D. Dunlop, G. Siefer, M. Yoshita, N. Kopidakis, K. Bothe, X. Hao, Solar cell efficiency tables (Version 61), Progress in Photovoltaics: Research and Applications. n/a (2022). https://doi.org/10.1002/pip.3646.

[5] Q. Jiang, X. Zhang, J. You, SnO2: A Wonderful Electron Transport Layer for Perovskite Solar Cells, Small. 14 (2018) 1801154. https://doi.org/10.1002/smll.201801154.

[6] Z.M. Jarzebski, J.P. Marton, Physical Properties of SnO2 Materials: II . Electrical Properties, J. Electrochem. Soc. 123 (1976) 299C. https://doi.org/10.1149/1.2133090.

[7] Z.M. Jarzebski, J.P. Morton, Physical Properties of SnO2 Materials: III . Optical Properties, J. Electrochem. Soc. 123 (1976) 333C. https://doi.org/10.1149/1.2132647.

[8] H. Min, D.Y. Lee, J. Kim, G. Kim, K.S. Lee, J. Kim, M.J. Paik, Y.K. Kim, K.S. Kim, M.G. Kim, T.J. Shin, S. Il Seok, Perovskite solar cells with atomically coherent interlayers on SnO2 electrodes, Nature. 598 (2021) 444–450. https://doi.org/10.1038/s41586-021-03964-8.

[9] J.J. Yoo, G. Seo, M.R. Chua, T.G. Park, Y. Lu, F. Rotermund, Y.-K. Kim, C.S. Moon, N.J. Jeon, J.-P. Correa-Baena, V. Bulović, S.S. Shin, M.G. Bawendi, J. Seo, Efficient perovskite solar cells via improved carrier management, Nature. 590 (2021) 587–593. https://doi.org/10.1038/s41586-021-03285-w.

[10] J. Barbé, M.L. Tietze, M. Neophytou, B. Murali, E. Alarousu, A.E. Labban, M. Abulikemu, W. Yue, O.F. Mohammed, I. McCulloch, A. Amassian, S. Del Gobbo, Amorphous Tin Oxide as a Low-Temperature-Processed Electron-Transport Layer for Organic and Hybrid Perovskite Solar Cells, ACS Appl. Mater. Interfaces. 9 (2017) 11828–11836. https://doi.org/10.1021/acsami.6b13675.

[11] E.H. Anaraki, A. Kermanpur, L. Steier, K. Domanski, T. Matsui, W. Tress, M. Saliba, A. Abate, M. Grätzel, A. Hagfeldt, J.-P. Correa-Baena, Highly efficient and stable planar perovskite solar cells by solution-processed tin oxide, Energy Environ. Sci. 9 (2016) 3128–3134. https://doi.org/10.1039/C6EE02390H.

[12] J.A. Smith, O.S. Game, J.E. Bishop, E.L.K. Spooner, R.C. Kilbride, C. Greenland, R. Jayaprakash, T.I. Alanazi, E.J. Cassella, A. Tejada, G. Chistiakova, M. Wong-Stringer, T.J. Routledge, A.J. Parnell, D.B. Hammond, D.G. Lidzey, Rapid Scalable Processing of Tin Oxide Transport Layers for Perovskite Solar Cells, ACS Appl. Energy Mater. 3 (2020) 5552–5562. https://doi.org/10.1021/acsaem.0c00525.

[13] Y. Ko, Y. Kim, C. Lee, T. Kim, S. Kim, Y.J. Yun, H. Gwon, N. Lee, Y. Jun, Self-Aggregation-Controlled Rapid Chemical Bath Deposition of SnO $_2$ Layers and Stable Dark Depolarization Process for Highly Efficient Planar Perovskite Solar Cells, ChemSusChem. 13 (2020) 4051–4063. https://doi.org/10.1002/cssc.202000501.

[14] M.J. Jeong, K.M. Yeom, S.J. Kim, E.H. Jung, J.H. Noh, Spontaneous interface engineering for dopant-free poly(3-hexylthiophene) perovskite solar cells with efficiency over 24%, Energy Environ. Sci. 14 (2021) 2419–2428. https://doi.org/10.1039/D0EE03312J.

[15] Y. Guo, X. Yin, J. Liu, W. Chen, S. Wen, M. Que, H. Xie, Y. Yang, W. Que, B. Gao, Vacuum thermal-evaporated SnO2 as uniform electron transport layer and novel management of perovskite intermediates for efficient and stable planar perovskite solar cells, Organic Electronics. 65 (2019) 207–214. https://doi.org/10.1016/j.orgel.2018.11.021.

[16] Z. Chen, G. Yang, X. Zheng, H. Lei, C. Chen, J. Ma, H. Wang, G. Fang, Bulk heterojunction perovskite solar cells based on room temperature deposited hole-blocking layer: Suppressed hysteresis and flexible photovoltaic application, Journal of Power Sources. 351 (2017) 123–129. https://doi.org/10.1016/j.jpowsour.2017.03.087.

[17] G. Bai, Z. Wu, J. Li, T. Bu, W. Li, W. Li, F. Huang, Q. Zhang, Y.-B. Cheng, J. Zhong, High performance perovskite sub-module with sputtered SnO2 electron transport layer, Solar Energy. 183 (2019) 306–314. https://doi.org/10.1016/j.solener.2019.03.026.

[18] H. Tao, H. Wang, Y. Bai, H. Long, H. Zhao, Q. Fu, Z. Ma, Effects of sputtering power of SnO2 electron selective layer on perovskite solar cells, J Mater Sci: Mater Electron. 30 (2019) 12036–12043. https://doi.org/10.1007/s10854-019-01561-0.

[19] J.P. Correa Baena, L. Steier, W. Tress, M. Saliba, S. Neutzner, T. Matsui, F. Giordano, T.J. Jacobsson, A.R. Srimath Kandada, S.M. Zakeeruddin, A. Petrozza, A. Abate, M.K. Nazeeruddin, M. Grätzel, A. Hagfeldt, Highly efficient planar perovskite solar cells through band alignment engineering, Energy Environ. Sci. 8 (2015) 2928–2934. https://doi.org/10.1039/C5EE02608C.

[20] S.M. George, Atomic Layer Deposition: An Overview, Chem. Rev. 110 (2010) 111–131. https://doi.org/10.1021/cr900056b.

[21] D.V. Nazarov, N.P. Bobrysheva, O.M. Osmolovskaya, M.G. Osmolovsky, V.M. Smirnov, Atomic Layer Deposition of Tin Dioxide Nanofilms: a Review, (2015) 14.

[22] M.N. Mullings, C. Hägglund, S.F. Bent, Tin oxide atomic layer deposition from tetrakis(dimethylamino)tin and water, Journal of Vacuum Science & Technology A: Vacuum, Surfaces, and Films. 31 (2013) 061503. https://doi.org/10.1116/1.4812717.

[23] J.W. Elam, D.A. Baker, A.J. Hryn, A.B.F. Martinson, M.J. Pellin, J.T. Hupp, Atomic layer deposition of tin oxide films using tetrakis(dimethylamino) tin, Journal of Vacuum Science & Technology A. 26 (2008) 244–252. https://doi.org/10.1116/1.2835087.

[24] V. Zardetto, B.L. Williams, A. Perrotta, F. Di Giacomo, M.A. Verheijen, R. Andriessen, W.M.M. Kessels, M. Creatore, Atomic layer deposition for perovskite solar cells: research status, opportunities and challenges, Sustainable Energy Fuels. 1 (2017) 30–55. https://doi.org/10.1039/C6SE00076B.

[25] P. Löper, B. Niesen, S.-J. Moon, S. Martín de Nicolas, J. Holovsky, Z. Remes, M. Ledinsky, F.-J. Haug, J.-H. Yum, S. De Wolf, C. Ballif, Organic–Inorganic Halide Perovskites: Perspectives for Silicon-Based Tandem Solar Cells, IEEE Journal of Photovoltaics. 4 (2014) 1545–1551. https://doi.org/10.1109/JPHOTOV.2014.2355421.

[26] Q. Wali, N.K. Elumalai, Y. Iqbal, A. Uddin, R. Jose, Tandem perovskite solar cells, Renewable and Sustainable Energy Reviews. 84 (2018) 89–110. https://doi.org/10.1016/j.rser.2018.01.005.

[27] Interactive Best Research-Cell Efficiency Chart, (n.d.). https://www.nrel.gov/pv/interactive-cell-efficiency.html (accessed March 7, 2023).

[28] T. Tiedje, E. Yablonovitch, G.D. Cody, B.G. Brooks, Limiting efficiency of silicon solar cells, IEEE Transactions on Electron Devices. 31 (1984) 711–716. https://doi.org/10.1109/T-ED.1984.21594.

[29] C. Wang, C. Xiao, Y. Yu, D. Zhao, R.A. Awni, C.R. Grice, K. Ghimire, I. Constantinou, W. Liao, A.J. Cimaroli, P. Liu, J. Chen, N.J. Podraza, C.-S. Jiang, M.M. Al-Jassim, X. Zhao, Y. Yan, Understanding and Eliminating Hysteresis for Highly Efficient Planar Perovskite Solar Cells, Advanced Energy Materials. 7 (2017) 1700414. https://doi.org/10.1002/aenm.201700414.

[30] Y. Lee, S. Lee, G. Seo, S. Paek, K.T. Cho, A.J. Huckaba, M. Calizzi, D. Choi, J.-S. Park, D. Lee, H.J. Lee, A.M. Asiri, M.K. Nazeeruddin, Efficient Planar Perovskite Solar Cells Using Passivated Tin Oxide as an Electron Transport Layer, Adv. Sci. 5 (2018) 1800130. https://doi.org/10.1002/advs.201800130.

[31] A.F. Palmstrom, J.A. Raiford, R. Prasanna, K.A. Bush, M. Sponseller, R. Cheacharoen, M.C. Minichetti, D.S. Bergsman, T. Leijtens, H.-P. Wang, V. Bulović, M.D. McGehee, S.F. Bent, Interfacial Effects of Tin Oxide Atomic Layer Deposition in Metal Halide Perovskite Photovoltaics, Advanced Energy Materials. 8 (2018) 1800591. https://doi.org/10.1002/aenm.201800591.

[32] Y. Kuang, V. Zardetto, R. van Gils, S. Karwal, D. Koushik, M.A. Verheijen, L.E. Black, C. Weijtens, S. Veenstra, R. Andriessen, W.M.M. Kessels, M. Creatore, Low-Temperature Plasma-Assisted Atomic-Layer-Deposited SnO2 as an Electron Transport Layer in Planar Perovskite Solar Cells, ACS Appl. Mater. Interfaces. 10 (2018) 30367–30378. https://doi.org/10.1021/acsami.8b09515.

[33] A. Hultqvist, T.J. Jacobsson, S. Svanström, M. Edoff, U.B. Cappel, H. Rensmo, E.M.J. Johansson, G. Boschloo, T. Törndahl, SnOx Atomic Layer Deposition on Bare Perovskite—An Investigation of Initial Growth Dynamics, Interface Chemistry, and Solar Cell Performance, ACS Appl. Energy Mater. 4 (2021) 510–522. https://doi.org/10.1021/acsaem.0c02405.

[34] A. Al-Ashouri, E. Köhnen, B. Li, A. Magomedov, H. Hempel, P. Caprioglio, J.A. Márquez, A.B. Morales Vilches, E. Kasparavicius, J.A. Smith, N. Phung, D. Menzel, M. Grischek, L. Kegelmann, D. Skroblin, C. Gollwitzer, T. Malinauskas, M. Jošt, G. Matič, B. Rech, R. Schlatmann, M. Topič, L. Korte, A. Abate, B. Stannowski, D. Neher, M. Stolterfoht, T. Unold, V. Getautis, S. Albrecht, Monolithic perovskite/silicon tandem solar cell with >29% efficiency by enhanced hole extraction, Science. 370 (2020) 1300–1309. https://doi.org/10.1126/science.abd4016.

[35] J. Liu, E. Aydin, J. Yin, M. De Bastiani, F.H. Isikgor, A.U. Rehman, E. Yengel, E. Ugur, G.T. Harrison, M. Wang, Y. Gao, J.I. Khan, M. Babics, T.G. Allen, A.S. Subbiah, K. Zhu, X. Zheng, W. Yan, F. Xu, M.F. Salvador, O.M. Bakr, T.D. Anthopoulos, M. Lanza, O.F. Mohammed, F. Laquai, S. De Wolf, 28.2%-efficient, outdoor-stable perovskite/silicon tandem solar cell, Joule. 5 (2021) 3169–3186. https://doi.org/10.1016/j.joule.2021.11.003.

[36] P. Tockhorn, J. Sutter, A. Cruz, P. Wagner, K. Jäger, D. Yoo, F. Lang, M. Grischek, B. Li, A. Al-Ashouri, E. Köhnen, M. Stolterfoht, D. Neher, R. Schlatmann, B. Rech, B. Stannowski, S. Albrecht, C. Becker, Nano-optical designs enhance monolithic perovskite/silicon tandem solar cells toward 29.8% efficiency, (2022). https://doi.org/10.21203/rs.3.rs-1439562/v1.

[37] F. Sahli, J. Werner, B.A. Kamino, M. Bräuninger, R. Monnard, B. Paviet-Salomon, L. Barraud, L. Ding, J.J. Diaz Leon, D. Sacchetto, G. Cattaneo, M. Despeisse, M. Boccard, S. Nicolay, Q. Jeangros, B. Niesen, C. Ballif, Fully textured monolithic perovskite/silicon tandem solar cells with 25.2% power conversion efficiency, Nature Mater. 17 (2018) 820–826. https://doi.org/10.1038/s41563-018-0115-4.

[38] M.F. Aygüler, A.G. Hufnagel, P. Rieder, M. Wussler, W. Jaegermann, T. Bein, V. Dyakonov, M.L. Petrus, A. Baumann, P. Docampo, Influence of Fermi Level Alignment with Tin Oxide on the Hysteresis of Perovskite Solar Cells, ACS Appl. Mater. Interfaces. 10 (2018) 11414–11419. https://doi.org/10.1021/acsami.8b00990.

[39] C. Wang, D. Zhao, C. R. Grice, W. Liao, Y. Yu, A. Cimaroli, N. Shrestha, P. J. Roland, J. Chen, Z. Yu, P. Liu, N. Cheng, R. J. Ellingson, X. Zhao, Y. Yan, Low-temperature plasma-

enhanced atomic layer deposition of tin oxide electron selective layers for highly efficient planar perovskite solar cells, Journal of Materials Chemistry A. 4 (2016) 12080–12087. https://doi.org/10.1039/C6TA04503K.

[40] J. Warby, F. Zu, S. Zeiske, E. Gutierrez-Partida, L. Frohloff, S. Kahmann, K. Frohna, E. Mosconi, E. Radicchi, F. Lang, S. Shah, F. Peña-Camargo, H. Hempel, T. Unold, N. Koch, A. Armin, F. De Angelis, S.D. Stranks, D. Neher, M. Stolterfoht, Understanding Performance Limiting Interfacial Recombination in pin Perovskite Solar Cells, Advanced Energy Materials. 12 (2022) 2103567. https://doi.org/10.1002/aenm.202103567.

[41] F.M. Rombach, S.A. Haque, T.J. Macdonald, Lessons learned from spiro-OMeTAD and PTAA in perovskite solar cells, Energy Environ. Sci. 14 (2021) 5161–5190. https://doi.org/10.1039/D1EE02095A.

[42] W. Ke, G. Fang, Q. Liu, L. Xiong, P. Qin, H. Tao, J. Wang, H. Lei, B. Li, J. Wan, G. Yang, Y. Yan, Low-Temperature Solution-Processed Tin Oxide as an Alternative Electron Transporting Layer for Efficient Perovskite Solar Cells, J. Am. Chem. Soc. 137 (2015) 6730–6733. https://doi.org/10.1021/jacs.5b01994.

[43] Q.-H. Wu, J. Song, J. Kang, Q.-F. Dong, S.-T. Wu, S.-G. Sun, Nano-particle thin films of tin oxides, Materials Letters. 61 (2007) 3679–3684. https://doi.org/10.1016/j.matlet.2006.12.016.

[44] B. Bob, T.-B. Song, C.-C. Chen, Z. Xu, Y. Yang, Nanoscale Dispersions of Gelled SnO2: Material Properties and Device Applications, Chem. Mater. 25 (2013) 4725–4730. https://doi.org/10.1021/cm402462m.

[45] M.A. Martínez-Puente, J. Tirado, F. Jaramillo, R. Garza-Hernández, P. Horley, L.G. Silva Vidaurri, F.S. Aguirre-Tostado, E. Martínez-Guerra, Unintentional Hydrogen Incorporation into the SnO2Electron Transport Layer by ALD and Its Effect on the Electronic Band Structure, ACS Applied Energy Materials. (2021). https://doi.org/10.1021/acsaem.1c01836.

[46] M. Batzill, U. Diebold, The surface and materials science of tin oxide, Progress in Surface Science. 79 (2005) 47–154. https://doi.org/10.1016/j.progsurf.2005.09.002.

[47] R. Scheer, H.-W. Schok, Appendix A: Frequently Observed Anomalies, in: Chalcogenide Photovoltaics, John Wiley & Sons, Ltd, 2011: pp. 305–314. https://doi.org/10.1002/9783527633708.ch7.

[48] P. Würfel, U. Würfel, Physics of Solar Cells: From Basic Principles to Advanced Concepts, 3rd ed., Wiley-VCH, 2016.

[49] C. Altinkaya, E. Aydin, E. Ugur, F.H. Isikgor, A.S. Subbiah, M.D. Bastiani, J. Liu, A. Babayigit, T.G. Allen, F. Laquai, A. Yildiz, S.D. Wolf, Tin Oxide Electron-Selective Layers for Efficient, Stable, and Scalable Perovskite Solar Cells, Advanced Materials. 33 (2021) 2005504. https://doi.org/10.1002/adma.202005504.

[50] M. Neukom, S. Züfle, S. Jenatsch, B. Ruhstaller, Opto-electronic characterization of third-generation solar cells, Science and Technology of Advanced Materials. 19 (2018) 291–316. https://doi.org/10.1080/14686996.2018.1442091.

[51] S. Jeong, S. Seo, H. Park, H. Shin, Atomic layer deposition of a SnO2 electron-transporting layer for planar perovskite solar cells with a power conversion efficiency of 18.3%, Chem. Commun. 55 (2019) 2433–2436. https://doi.org/10.1039/C8CC09557D.

[52] N. Guan, C. Ran, Y. Wang, L. Chao, Z. Deng, G. Wu, H. Dong, Y. Bao, Z. Lin, L. Song, SnO2 Passivation and Enhanced Perovskite Charge Extraction with a Benzylamine Hydrochloric Interlayer, ACS Appl. Mater. Interfaces. (2021). https://doi.org/10.1021/acsami.1c17788.

[53] A. M. Ganose, D. O. Scanlon, Band Gap and Work Function Tailoring of SnO 2 for Improved Transparent Conducting Ability in Photovoltaics. Journal of Materials Chemistry C 2016, 4 (7), 1467− 1475.

[54] M. N. Islam, O. M. Hakim, M. OElectron Affinity and Work Function of Polycrystalline SnO2 Thin Film. J. Mater. Sci. Lett. 1986, 5 (1), 63−65.

[55] S. Béchu, M. Ralaiarisoa, A. Etcheberry, P. Schulz, Photoemission Spectroscopy Characterization of Halide Perovskites, Advanced Energy Materials. n/a (2020) 1904007. https://doi.org/10.1002/aenm.201904007.

[56] T. Hu, T. Becker, N. Pourdavoud, J. Zhao, K.O. Brinkmann, R. Heiderhoff, T. Gahlmann, Z. Huang, S. Olthof, K. Meerholz, D. Többens, B. Cheng, Y. Chen, T. Riedl, Indium-Free Perovskite Solar Cells Enabled by Impermeable Tin-Oxide Electron Extraction Layers, Advanced Materials. 29 (2017) 1606856. https://doi.org/10.1002/adma.201606856.

[57] D. Regaldo, A. Bojar, S. P. Dunfield, P. Lopez-Varo, M. Frégnaux, V. Dufoulon, S.-T. Zhang, J. Alvarez, J. J. Berry, J.-B. Puel, P. Schulz, J.-P. Kleider, On the Equilibrium Electrostatic Potential and Light-Induced Charge Redistribution in Halide Perovskite Structures. Progress in Photovoltaics: Research and Applications 2022, 30 (8), 994−1002.

[58] P. Schulz, L.L. Whittaker-Brooks, B.A. MacLeod, D.C. Olson, Y.-L. Loo, A. Kahn, Electronic Level Alignment in Inverted Organometal Perovskite Solar Cells, Advanced Materials Interfaces. 2 (2015) 1400532. https://doi.org/10.1002/admi.201400532.

[59] P. Fassl, V. Lami, A. Bausch, Z. Wang, M.T. Klug, H.J. Snaith, Y. Vaynzof, Fractional deviations in precursor stoichiometry dictate the properties, performance and stability of perovskite photovoltaic devices, Energy Environ. Sci. 11 (2018) 3380–3391. https://doi.org/10.1039/C8EE01136B.

[60] I. Levine, K. Shimizu, A. Lomuscio, M. Kulbak, C. Rehermann, A. Zohar, M. Abdi-Jalebi, B. Zhao, S. Siebentritt, F. Zu, N. Koch, A. Kahn, G. Hodes, R.H. Friend, H. Ishii, D. Cahen, Direct Probing of Gap States and Their Passivation in Halide Perovskites by High-Sensitivity, Variable Energy Ultraviolet Photoelectron Spectroscopy, J. Phys. Chem. C. 125 (2021) 5217–5225. https://doi.org/10.1021/acs.jpcc.0c11627.

[61] S. Das, V. Jayaraman, SnO2: A comprehensive review on structures and gas sensors, Progress in Materials Science. 68 (2014) 112–255. https://doi.org/10.1016/j.pmatsci.2014.06.003.

[62] A. Schleife, J.B. Varley, F. Fuchs, C. Rödl, F. Bechstedt, P. Rinke, A. Janotti, C.G. Van de Walle, Tin dioxide from first principles: Quasiparticle electronic states and optical properties, Phys. Rev. B. 83 (2011) 035116. https://doi.org/10.1103/PhysRevB.83.035116.

[63] D. Choi, W.J. Maeng, J.-S. Park, The conducting tin oxide thin films deposited via atomic layer deposition using Tetrakis-dimethylamino tin and peroxide for transparent flexible electronics, Applied Surface Science. 313 (2014) 585–590. https://doi.org/10.1016/j.apsusc.2014.06.027.

[64] J. Tauc, Optical properties and electronic structure of amorphous Ge and Si, Materials Research Bulletin. 3 (1968) 37–46. https://doi.org/10.1016/0025-5408(68)90023-8.

[65] K. Rajshekar, K. Dhanaraj, A Comprehensive Density-of-States Model for Oxide Semiconductor Thin Film Transistors, In Review, 2021. https://doi.org/10.21203/rs.3.rs-236842/v1.

[66] I. Hamberg, C.G. Granqvist, K.-F. Berggren, B.E. Sernelius, L. Engström, Band-gap widening in heavily Sn-doped In 2 O 3, Phys. Rev. B. 30 (1984) 3240–3249. https://doi.org/10.1103/PhysRevB.30.3240.

[67] G. Sanon, R. Rup, A. Mansingh, Band-gap narrowing and band structure in degenerate tin oxide (SnO 2) films, Phys. Rev. B. 44 (1991) 5672–5680. https://doi.org/10.1103/PhysRevB.44.5672.

[68] S.P. Harvey, Z. Li, J.A. Christians, K. Zhu, J.M. Luther, J.J. Berry, Probing Perovskite Inhomogeneity beyond the Surface: TOF-SIMS Analysis of Halide Perovskite Photovoltaic Devices, ACS Appl. Mater. Interfaces. 10 (2018) 28541–28552. https://doi.org/10.1021/acsami.8b07937.

[69] S.P. Harvey, F. Zhang, A. Palmstrom, J.M. Luther, K. Zhu, J.J. Berry, Mitigating Measurement Artifacts in TOF-SIMS Analysis of Perovskite Solar Cells, ACS Appl. Mater. Interfaces. 11 (2019) 30911–30918. https://doi.org/10.1021/acsami.9b09445.

[70] N. Lee, J.H. Bang, H.W. Kim, H. Jeon, New approach to SnO2-based transparent conducting oxides incorporating synergistic effects of Au nano particles and microwave irradiation, Ceramics International. 47 (2021) 10628–10634. https://doi.org/10.1016/j.ceramint.2020.12.175.

[71] S. Evans, J.M. Thomas, Electronic structure of the oxides of lead. Part 1.—A study using X-ray and ultraviolet photoelectron spectroscopy of the oxidation of polycrystalline lead, J. Chem. Soc., Faraday Trans. 2. (1975) 313–328. https://doi.org/10.1039/F29757100313.

[72] X-ray Photoelectron Spectroscopy (XPS) Reference Pages, (n.d.). http://www.xpsfitting.com/search/label/Oxygen (accessed September 24, 2022).

[73] V.B. Crist, Lead (Pb), Z=82, & Lead Compounds, The International XPS Database. (2022). https://xps-database.com/lead-pb-z82-lead-compounds/ (accessed October 20, 2022).

[74] M. Fondell, M. Gorgoi, M. Boman, A. Lindblad, An HAXPES study of Sn, SnS, SnO and SnO2, Journal of Electron Spectroscopy and Related Phenomena. 195 (2014) 195–199. https://doi.org/10.1016/j.elspec.2014.07.012.